

Entropy Regularized Deconvolution of Cellular Cryo-Transmission Electron Tomograms

Matthew Croxford^a, Michael Elbaum^b, Muthuvel Arigovindan^c, Zvi Kam^d, David Agard^e, Elizabeth Villa^{a*}, and John Sedat^{e*}

^aSection of Molecular Biology, Division of Biological Sciences, University of California, San Diego, 92093; ^bDepartment of Chemical and Biological Physics Weizmann Institute of Science, Rehovot 760001, Israel; ^cDepartment of Electrical Engineering, Indian Institute of Science, Bengaluru - 560012; ^dDepartment of Molecular Cell Biology, Weizmann Institute of Science, Rehovot 760001, Israel; ^eDepartment of Biochemistry and Biophysics University of California, San Francisco, Ca. 94158 USA

This manuscript was compiled on May 3, 2021

1 **Cryo-electron tomography (cryo-ET) allows for the high resolution visualization of biological macromolecules. However, the technique is**
2 **limited by a low signal-to-noise ratio (SNR) and variance in contrast at different frequencies, as well as reduced Z resolution. Here, we**
3 **applied entropy regularized deconvolution (ER DC) to cryo-electron tomography data generated from transmission electron microscopy**
4 **(TEM) and reconstructed using weighted back projection (WBP). We**
5 **applied DC to several *in situ* cryo-ET data sets, and assess the results by Fourier analysis and subtomogram analysis (STA).**

Cryo-Electron Tomography | Deconvolution | Subtomogram Analysis | Structural Biology | Missing Wedge

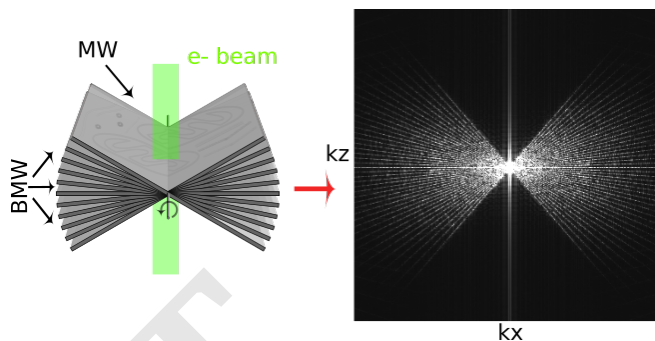


Fig. 1. Tilt series collection and the missing wedge issue. Left: Schematic of tilt-series collection scheme. Sample projections are acquired over a range of tilt angles, typically from -60° to $+60^\circ$. Right: Middle slice of the $kxkz$ plane shows the missing wedge (MW) and baby missing wedges (BMW) of information visualized in Fourier space.

wedge. The gaps between discrete tilt angles also leave small missing wedges as seen in Fig. 1. Since the reconstruction is equivalent to an inversion in Fourier space, it is obvious that some interpolation is required and that the data are incomplete. As such, it is not surprising that different algorithms can generate somewhat different reconstructions from the same data. Commonly recognized artifacts are elongation along the Z direction and streaks projecting from high contrast points into neighboring planes in the volume.

In addition to the missing wedges, TEM images require a significant defocus to get adequate contrast. For *in situ* cryo-ET data, a typical defocus of at least $5\ \mu\text{m}$ is used. Finally, the process of reconstruction by weighted back projection (WBP) introduces well-known problems. These include significant intensity above and below the sample volume, where we expect

Significance Statement

Cellular cryo-electron tomography suffers from severely compromised Z resolution due to the missing wedges of information not collected during the acquisition of tilt series. This paper shows that application of entropy regularized deconvolution (ER DC) to TEM tomography, substantially fills in this missing information, allowing for improved Z resolution and better interpretation of cellular structures.

J.S. and E.V. designed the project, E.V. lab acquired data, M.C. and J.S. performed data processing and analysis. E.V., J.S., M.E., M.A., Z.K. and D.A. gave insightful input at different stages of the project. M.C. and J.S. wrote the paper with input from all authors.

The authors declare no conflict of interest in this research.

* To whom correspondence should be addressed. E-mail: evilla@ucsd.edu, sedat@msg.ucsf.edu

1 **R**ecent advances in cryo-electron tomography (cryo-ET),
2 most notably the ability to thin cryo-preserved specimens
3 using a focused ion beam (FIB), have opened windows for
4 the direct visualization of the cell interior at nanometer-scale
5 resolution (1–9). Cells are rapidly frozen to achieve a vitreous
6 form of ice that preserves biological molecules in a near-native
7 state. They are then cryo-FIB milled to a suitable thickness of
8 100–350 nm for imaging with transmission electron microscopy
9 (TEM). A series of projection images is acquired, typically
10 with 1–5 degree increments and then reconstructed into a 3D
11 volume (10). This 3D reconstruction is rendered for display
12 and analysis, which may entail segmentation to highlight extended
13 structures or averaging of sub-volumes for enhancement of
14 molecular-scale resolution (11, 12).

15 While cryo-ET offers unparalleled resolution of cellular
16 interiors, it is challenging for a number of reasons. First,
17 vitrified biological samples are highly sensitive to damage by
18 the electron irradiation required for imaging. Constraints on
19 the permissible exposure result in limited contrast and a low
20 signal to noise ratio (13). Second, the modality of wide-field
21 TEM depends on defocus to generate useful phase contrast,
22 but with a non-trivial dependence on spatial frequency that is
23 expressed in a contrast transfer function (CTF). Contrast is
24 lost at low spatial frequencies and oscillates at high spatial frequencies,
25 meaning that material density could be represented as
26 intensity either darker or lighter than background (14–16).
27 Post-processing is applied to correct this representation in the
28 image intensities. The correction is inherently approximate,
29 and is especially challenging in tomography where the defocus
30 varies across the field of view (17). Third, the available raw
31 data are never sufficient to produce an unambiguous reconstruction.
32 The tilt range is restricted by the slab geometry, typically
33 to about 120° around the vertical. The projected thickness
34 of a slab also increases with tilt angle, resulting in degraded
35 contrast and resolution from these contributions to the reconstruction.
36 The missing information is best recognized in Fourier space,
37 where it is known as the missing

53 vacuum with no signal. This is due to cross-terms in the WBP
 54 coming from the tilt wedges, as well as distortions in the WBP
 55 arising from the missing wedge. Because of these issues with
 56 cryo-ET data, filters to improve contrast and compensate for
 57 the missing wedge are an area of ongoing research (18). These
 58 techniques include non-linear anisotropic diffusion (NAD),
 59 convolutional neural networks based on detector noise models,
 60 wavelet based filtering methods, different implementations
 61 of deconvolution, and model based iterative reconstruction
 62 (MBIR) (19–28). Here, we present a deconvolution approach to
 63 achieve both enhanced SNR and missing wedge compensation.

64 The image distortions resulting from the incomplete tilt series and CTF can be characterized in terms of a single sample point of the data. This model is referred to as the point spread function (PSF), of which the hour-glass PSF in light microscopy is a classical example (29–31). Formally, the PSF is convolved with all points in the specimen function to form what is recorded in the image (32). If the PSF is well defined, it becomes possible to partially reverse the process of convolution to obtain an improved reconstruction. This reversal is referred to as deconvolution, which is a mathematical/computational iterative inversion processing procedure, extensively utilized in astronomy, spectroscopy, and light microscopy to partially restore data distorted by the imaging process (32). The deconvolution process is constrained. The most common constraint is the imposition of positivity of the deconvolved data (32). Other stabilizing constraints may include smoothing in real space to suppress high-frequency oscillations. DC is also very sensitive to noise, and most DC algorithms include regularization parameters whose values are difficult to evaluate theoretically. Additionally, in most cases the DC algorithms will diverge with increasing iterations, building up mottle and noise that obscure the interpretation of the final DC image. Finally, most DC implementations do not have a practical estimate of the error in the converged solution.

88 Entropy-regularized deconvolution ER-DC (33) is formulated to handle data with a weak signal to noise ratio, with a regularization term that exploits certain characteristics specific to images originating from cell organelles. Specifically, in cellular images, high intensities and high second-order derivatives exhibit certain sparse distribution, and this property is exploited by the custom regularization used in ER-DC. This regularization was originally designed for fluorescence images, and this approach was taken recently for processing of STEM cryo-tomography (CSTET) reconstructions (26). It is similar to deconvolution applied to fluorescence microscopy, where out of focus light creates a haze, but differs in that the artifacts to be removed originate primarily in the reconstruction rather than the optics. Whereas the individual 2D image is treated as a bona fide 2D projection, the kernel of the deconvolution was taken as the sum of the illumination profiles used in the tilt series. However, since TEM is currently the dominant modality for biological 3-D imaging of cells (34) and its CTF is complex, this deserves a separate study, which is the focus of this paper. The major distinction is that the contrast inversions, which were absent in the STEM data as acquired for tomography, should be accommodated in construction of the 3D PSF for TEM tomography.

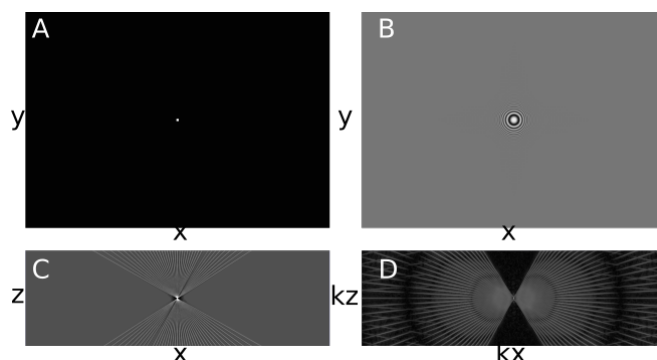


Fig. 2. Generating the TEM Point Spread Function. (A) Synthetic tilt series of a centered point source. (B) Point source tilt series convolved with CTF. (C) Slice of the weighted back projection tomogram of convolved CTF-point source (PSF), xz view. (D) 3D FFT of tomogram showed in C, xz slice.

Results

Electron Tomography Point Spread Function. The key to a meaningful deconvolution is that the synthetic PSF should represent as closely as possible the 3D image of an ideal point source. In the case of TEM, this requires an accounting for the defocus imposed in the image acquisition, which is customarily expressed in terms of a contrast transfer function (CTF). The 3D PSF for deconvolution was computed from simulated projections of a point source with the same dimensions and pixel spacing as the aligned tilt series (Fig. 2A). The CTF was first convolved with a projected point-source (Fig. 2B), and then a synthetic tilt series was reconstructed to the same dimensions as the original tomogram using the tilt angles represented in the corresponding reconstruction (Fig. 2C). This is the real-space PSF, whose 3D FFT serves as the optical transfer function, or kernel, for the deconvolution (Fig 2D). In principle, the 2D original CTFs vary with the gradient of defocus of the reconstructed volume. For simplicity, in this first demonstration we limited the analysis to a single nominal defocus and a spatially-invariant deconvolution kernel. A flow diagram for the PSF process is shown in (SI Appendix Fig. S1).

Tomogram Deconvolution. As a first demonstration of the TEM deconvolution we used a HEK cell cultured on-grid that had been FIB-milled to 150 nm thickness. The reconstructed volume contains membranes, microtubules, and a prominent crystalline protein array. The cells were overexpressing human Parkinson's related protein LRRK2-I2020T (35), and the observed repetitive structure is likely an autophagosome, given its double lipid bilayer structure (36). Contrast is sharp in slices through the XY plane of the tomogram, as expected (blue plane-mid structure, Fig. 3B), but contrast and resolution in the Z direction, seen in a slice through the XZ plane (orthogonal green plane in mid structure, Figure 3C) are severely compromised. Furthermore, the reconstructed volume displays a signal both above and below the specimen when observed in the XZ plane. Since the milled slab of material is finite in the z direction, and the sample is imaged in a vacuum, there should be negligible intensity outside it in the reconstructed data. This is a known artifact of back projection. These image distortions in real space can also be characterized in Fourier space, where the real space dimensions (x, y, z) correspond

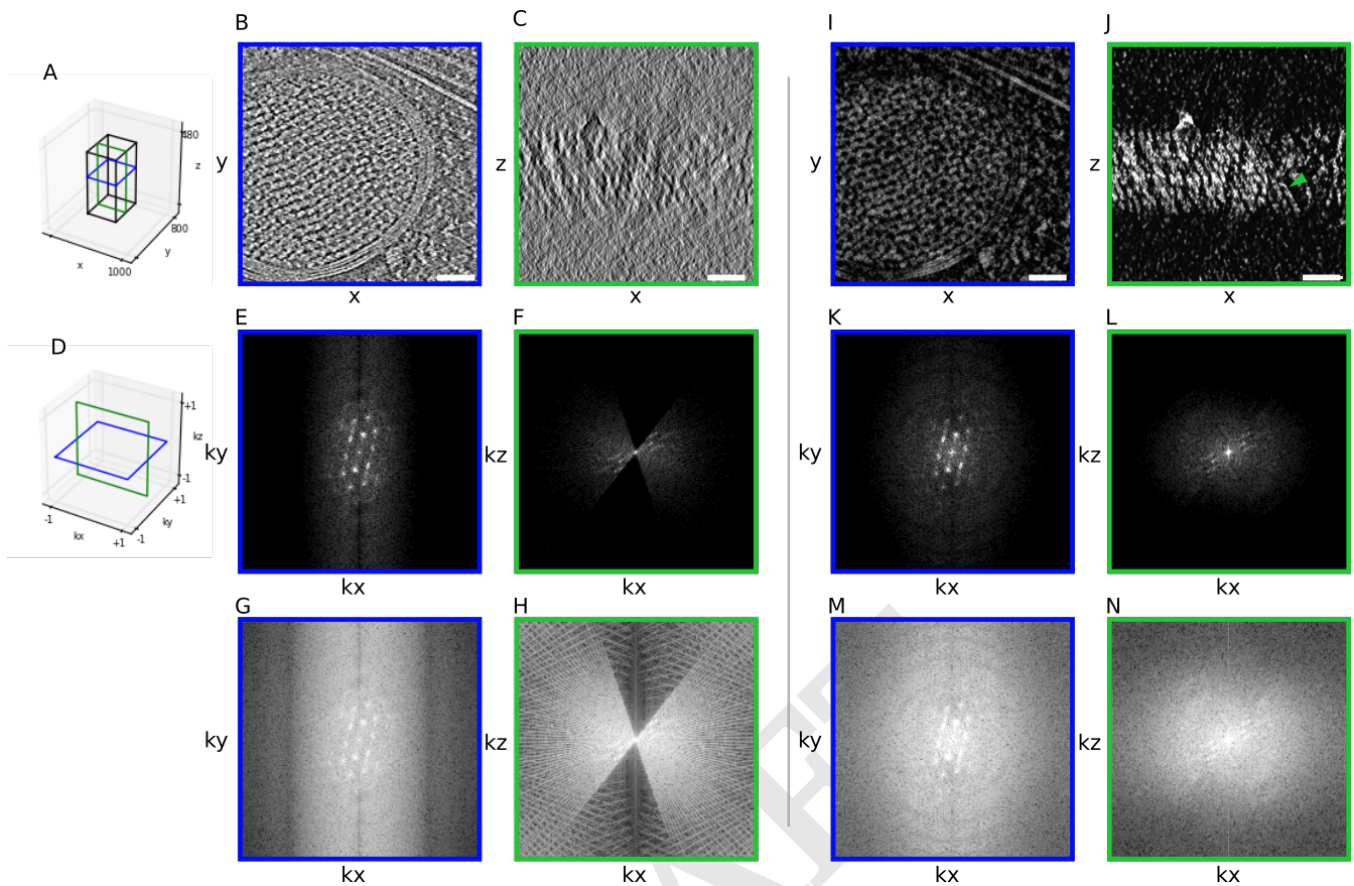


Fig. 3. Filling of Missing Wedge by Deconvolution (A) Schematic of slices used to generate panels B, C, I and J. (B) XY Slice of a tomogram of a HEK cell reconstructed using back projection. Throughout this work, white intensities correspond to high density values. (C) XZ slice of the same tomogram. (D) Schematic to show slices through Fourier space used to generate E,G,K,M in blue and F,H,M,L,M in green. (E,G) Slice through 3D FFT of the back projection corresponding to XY shown with a different distribution of voxel intensities. (F,H) Slice through 3D FFT of the back projection corresponding to XZ shown at two different intensity scales. (I-N) Corresponding results for the tomogram after deconvolution including a spatial constraint. Scale bars: 100 nm.

153 to the Fourier dimensions (K_x, K_y, K_z). The protein array
 154 in the real space XY plane appears as a lattice of calculated
 155 diffraction spots in the plane (K_x, K_y), as expected (Figure
 156 3E). In the XZ plane, the lattice of spots is sharply truncated
 157 at the Fourier planes normal to the limits of the acquired tilts.
 158 In summary, back projection suffers from major distortions
 159 visible in both real and Fourier space.

160 The result of 3D deconvolution processing is shown along-
 161 side the reconstruction in Figure 3. Full details appear in the
 162 supporting information. All processing was performed using
 163 PRIISM image processing software (37). Briefly, the entropy-
 164 regularized deconvolution algorithm from PRIISM was applied
 165 using the simulated PSF. In addition to imposing a penalty on
 166 negative intensities (positivity constraint), a spatial constraint
 167 was added to the error function on each iteration in order to
 168 penalize for spurious intensity reconstructed above and below
 169 the specimen volume. While contrast is enhanced in the XY
 170 plane, the more striking improvement is seen in the XZ plane
 171 (Fig. 3J), in comparison with the back projection (Fig. 3C).
 172 In the deconvolved tomogram, two lipid bilayers are visible
 173 (arrow) across the entire sample along Z, as is the crystalline
 174 array (Fig. 3J). The restoration of information along Z in
 175 real space can also be seen in the 3D Fourier transform of
 176 the deconvolved volume, which shows increased signal in the
 177 previously empty regions corresponding to the missing wedges

(Fig. 3F,L).

178 A very effective way to observe the results of DC is to
 179 study a small volume of the WBP and/or DC in a dynamic
 180 interacting display module, typically a video of the rotating
 181 volume. Stereo pairs with additional rotated views are shown
 182 for the WBP and DC (SI Appendix videos 1 and 2). These
 183 may be rocked with a cursor bar, as described in supporting
 184 information, in order to gain an impression in 3D. Distortions
 185 along the Z axis associated with the WBP are largely removed
 186 after DC processing, with a visual improvement in resolution
 187 along Z. **Resolution in the deconvolution can be esti-
 188 mated by analysis of the Fourier transform as shown
 189 by the data (Figure S2).** Significant information appears
 190 in the power spectrum appears beyond a spatial frequency
 191 of approximately 2.5 nm, which corresponds nominally to the
 192 second zero in the CTF for 6 micron defocus.
 193

194 **A Second Deconvolution Example.** For a second example, we
 195 applied ER-DC to a tomogram of a relatively thick lamella of *S.*
 196 *cerevisiae* cells (370 nm). Besides the thickness, cryo-electron
 197 tomography data of nuclei are challenging samples to interpret
 198 as nuclei are densely packed, and lack high-contrast features
 199 like membranes and cytoskeletal elements. As with the DC of
 200 mammalian cells, DC provided increased contrast in XY and
 201 an improved ability to visually interpret information along

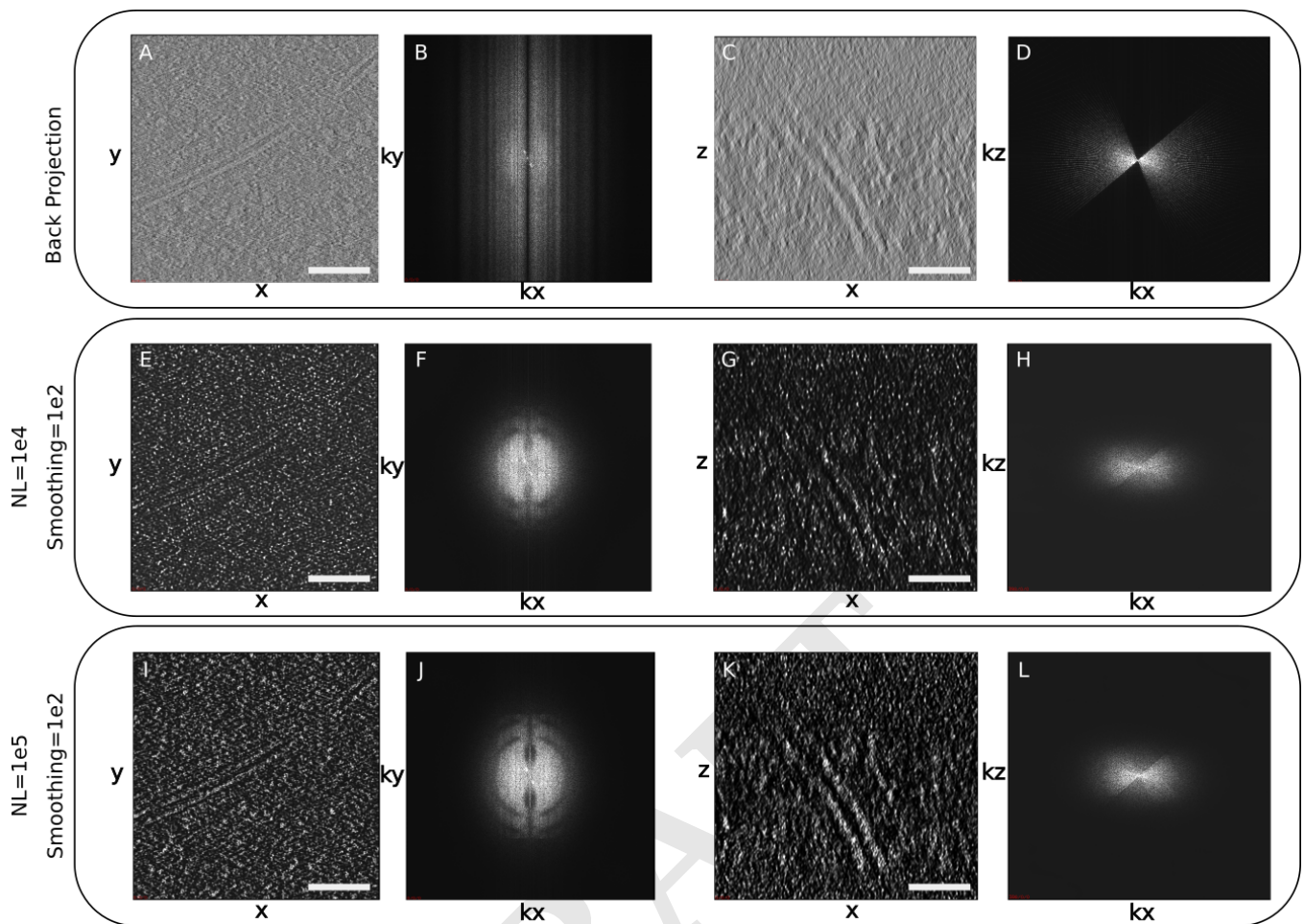


Fig. 4. Deconvolution of a Tomogram of the Nuclear Periphery of a Yeast Cell. (A) Central slice (10.62 nm thick) of the XY plane of a WBP tomogram of the nuclear periphery of a *S. cerevisiae* cell. (B) Fourier transform of A. (C) Central slice of the XZ plane of a WBP tomogram. (D) Fourier transform of C. (E) Central slice of the XY plane of a tomogram from A, deconvolved with a smoothing parameter of $1e2$ and a non-linearity factor of 10,000. (F) Fourier transform of E. (G) Central slice of the XZ plane of the deconvolved tomogram from E. (H) Fourier transform of G. (I) 10.6 nm slice of the XY plane of a tomogram from A, deconvolved with a smoothing parameter of $1e2$ and a non-linearity factor of 100,000. (J) Fourier transform of I. (K) 10.6 nm slice of the XZ plane of the deconvolved tomogram from I. (L) Fourier transform of K. Scale bars: 100 nm

202 Z compared to the back projection. The nuclear envelope is
 203 clearly visible in the XY slices of the WBP and the two DCs
 204 (Fig. 4 A, E, I). In XZ however, no clear structure can be
 205 followed in the BP (Fig. 4C), but can be more easily followed
 206 in the DC (Fig. 4 G, K). Additionally, the missing wedge
 207 seen in Fourier space is filled in by the DC process (Fig. 4 H,
 208 L). By utilizing rotating angle stereo-pair renderings of the
 209 volume (RAPSSs), one can compare the WBP and DC volumes
 210 in 3D (SI Appendix videos 3 and 4). In the BP, there is little
 211 distinguishable structure as the volume rotates. In contrast,
 212 fine features can be identified at every angle, such as the
 213 nuclear envelope, as well as densities that could correspond
 214 to chromatin and nucleosomes. The 3D-FFT of the DC (Fig. 4),
 215 KxKz view, shows the missing wedges being filled in, indicating
 216 that the DC process helps correct for these artifacts, even in
 217 challenging samples.

218 **Deconvolution and Subtomogram Analysis.** Subtomogram
 219 analysis is an approach to protein structure determination
 220 *in situ* (11, 38–52). Similarly to single particle analysis, of
 221 which it is an extension to 3D, averaging multiple examples
 222 of identical images serves to reduce noise. 3D averaging can

also be used to compensate for the missing wedge in a given
 tomogram acquisition if the molecules lie in random orientations
 (11). The crystalline-like body seen in Fig. 3 provided an
 interesting test case for averaging where orientations were
 determined uniformly by translational symmetry in the crystal
 (Fig. 5). Therefore only select orientations are available for
 view. First, we attempted to align the crystal subunits over
 360° in θ and ϕ on the WBP reconstruction. This resulted
 in an average that was dominated by the missing wedge, a
 common pitfall in sub-tomogram averaging, and produced a
 structure that was strongly elongated in the view direction
 (Fig. 5A). Second, we used the same particles, but this time
 from the deconvolved data set, aligned and averaged them with
 a resulting structure that resembled much better the unit of
 the crystalline array in the original tomogram (Fig. 5E). Third,
 we averaged the WBP particles using the DC alignment trans-
 formations. In this last case, we obtained a structure similar
 to the one obtained from DC-aligned and DC-averaged particles
 (SI Appendix Fig. 4B). This is a very practical realization
 of the improved axial resolution in the DC, or equivalently
 the suppression of the missing wedge artifact in the WBP
 data, demonstrating that the alignment of subtomograms is

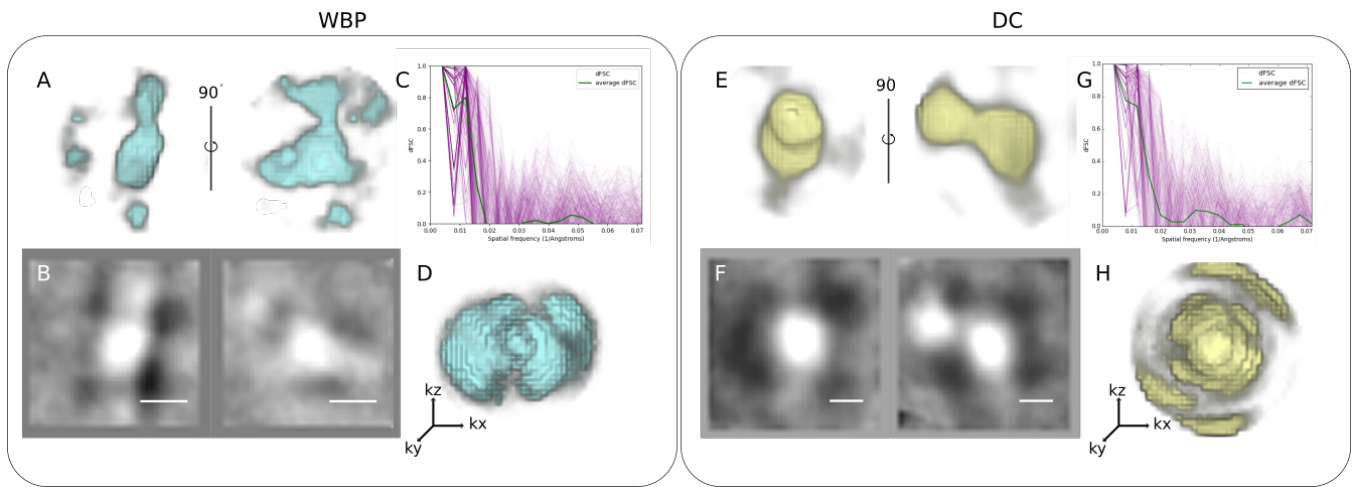


Fig. 5. Back projection vs deconvolution crystal body averages. (A) Two views of the crystal body average of WBP subtomograms. (B) Central 3.5nm slice of WBP crystal body subtomogram average. (C) 3D-FSC curves generated from two half-map averages of the WBP crystal body subtomogram average. Green line is the average, pink lines are individual directional FSCs. (D) 3D render of directional FSC curves. (E-H) corresponding averages and FSCs derived from the DC volume. Scale bars: 10 nm

245 improved by DC. This tomogram was acquired from a HEK
 246 cell overexpressing human LRRK2 (35). While the identity
 247 of the molecules forming the crystalline-like array was not
 248 specifically established (e.g., by CLEM) and the number of
 249 particles in this tomogram is severely limited (82), the DC
 250 average resembles the cryo-EM structures of LRRK2 determined
 251 both *in situ* bound to microtubules (35) and *in vitro* (53).

252 Fourier shell correlation (FSC) is widely used in single particle
 253 cryo-EM (54), as a metric of the resolution of a molecular
 254 structure. It is a quantitative measure of similarity, typically
 255 implemented in cryo-EM by comparing two structures, each
 256 generated from a half dataset. Standard FSC compares global
 257 similarities, giving a single curve for the entire structure, showing
 258 the correlation score as a function of spatial frequency.
 259 Resolution is then quoted as the inverse spatial frequency
 260 where the correlation drops below an accepted threshold. Directional
 261 FSC (dFSC) is a variant in which all Euler angles are
 262 explored for frequency comparison, and provides a representation
 263 of resolution in all directions (55). dFSC was applied
 264 to two half-map averages of the crystalline arrays from the
 265 WBP, and then to the DC averages to assess any change in
 266 resolution in any direction between the WBP (Fig. 5 C) and
 267 DC (Fig. 5G). Both averaged correlation curves drop to near
 268 zero by a frequency of $1/.02 \text{ \AA}^{-1}$, implying a resolution on
 269 the order of 5 nm. However there is a striking difference in the
 270 degree of anisotropy as a function of direction in the WBP;
 271 in the DC curves most of the directional correlation lines run
 272 nearly parallel. This is also reflected in the isosurfaces shown
 273 in Figure 5D and H.

274 To investigate the effects of DC in the alignment of the
 275 particles and the improvement of the average due to the missing
 276 wedge separately, we chose to use microtubules, since their
 277 structure is well established, as are the pipelines for
 278 subtomogram analysis. We analyzed a tomogram of reconstituted
 279 microtubules decorated by the Parkinson's related protein
 280 LRRK2^{RCKW} (53). In the tomogram, it is evident that the
 281 deconvolution process increased the contrast between the
 282 microtubules and the surrounding media, and we again see
 283 a reduction in XZ distortions (Fig. 6A,B,D,E), as well as a
 284 corresponding filling of information in the missing wedge in

285 Fourier space (Fig. 6C, F). Microtubule subtomograms were
 286 extracted from both the WBP and DC volumes using the
 287 filament tracing function in Dynamo(56). The subtomograms
 288 were independently aligned and averaged as described in (35)
 289 (Fig. 7 A, B). Note that the contrast between protofilaments
 290 is distinctly sharper for the DC data. However, this method of
 291 alignment includes an azimuthal randomization that is specifically
 292 designed to cancel out the missing wedge in the final
 293 average. To assess the effect of DC specifically on the missing
 294 wedge, we also ran the alignment on particles without this
 295 randomization step. Compared to the WBP, the DC-processed
 296 average shows more distinctly visible protofilaments in the
 297 direction of the missing wedge (Fig. 7E). Last, we used the DC
 298 alignment parameters to average the WBP particles (Fig. 7F).
 299 Here, the average still shows a prominent missing wedge. Thus,
 300 the DC improves both the alignment and the averaging steps
 301 of subtomogram analysis.

302 Discussion

303 We have successfully applied ER DC to cryo-electron tomograms,
 304 and demonstrated enhanced contrast compared to the back
 305 projection reconstructions, as well as less distorted structures
 306 along the Z axis. In real space, one can follow membranes
 307 in the XZ plane of the deconvolved volume, that were hardly
 308 visible in the back projection. In Fourier space, it is clear
 309 that portions of the missing wedge are filled in, and the
 310 distribution of voxel intensities changes significantly as a result
 311 of deconvolution. However, there are still several considerations
 312 for TEM deconvolution, and these are further discussed in the
 313 supporting information.

314 First, the reality is that DC acts as a filter for the data.
 315 The intensity of each voxel is modified in some fashion, and
 316 care must be taken in interpreting the DC volume. DC has two
 317 parameters, for non-linearity and smoothness, and the optimal
 318 values must be determined experimentally by systematically
 319 varying the parameters over several orders of magnitude; the
 320 parameter search quickly settles into basic convergent DC
 321 images that look biologically reasonable (e.g. membrane bilayers
 322 are visible, ribosomes are distinct, etc.) At the end of the DC
 323 process, one can usually settle on a few DC images coming

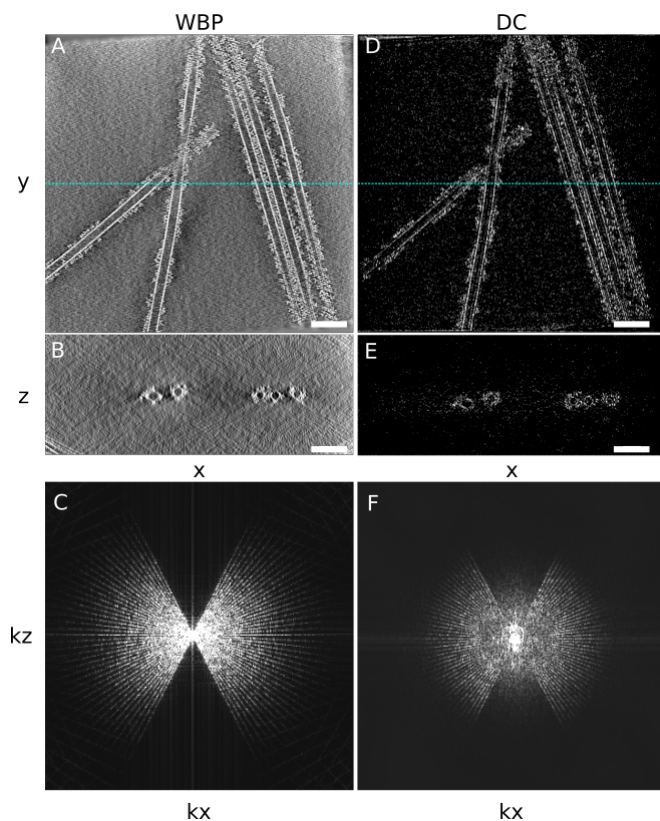


Fig. 6. Deconvolution of a tomogram of reconstituted microtubules. (A) XY slice of the WBP-reconstructed tomogram containing microtubules. (B) XZ view of the tomogram in A; blue dashed line in A corresponds to the slice shown. (C) kxkz view showing the missing wedge. (D) XY of the deconvolved tomogram. (E) XZ of deconvolved microtubule tomogram in D; blue dashed line in D corresponds to the slice shown. (F) kxkz of the deconvolved tomogram. Scale bar = 50 nm

observed data, into their correct structural space. Since all image information can be decomposed into 3-dimensional Fourier representation, one is, in essence, saying that there is information in one region of Fourier space that can be extrapolated correctly into other regions of Fourier space by the DC process. There are two examples from the inverse problems literature to reassure that such extrapolated information can indeed be real. The first one is called “Analytical Continuation” ((57), and references therein), which is known in optics literature. The Analytical Continuation (AC) conjecture, taken from (57), states: All image information can be decomposed into a Fourier transform, and a spatially bounded region of Fourier space can be expressed as an analytical function. The analytical function can be exactly known for a small region, and if there is no noise, the entire analytical function can be determined/extrapolated by AC. The extension can continue indefinitely, and this is a hallmark of AC (57). Noise is critical and the analytical values become small as iterations progress as the function get extended to higher resolution regions of Fourier space, reasons AC is little used (but see (57)). In the case of ER DC, noise is heavily suppressed and resolution extensions required are modest, suggesting that AC might work.

The second one is called compressive sensing reconstruction, used in modalities such as magnetic resonance imaging (58) and tomography (59). It involves high-quality reconstruction from highly under-sampled Fourier data and tomographic projections with a limited set of angles with regularization constructed using derivatives. Because of the way the derivative operator is related to the measurement operator (tomographic projection or Fourier transformation), high quality reconstruction becomes possible from sparse Fourier samples or from tomographic projections from a limited set of angles. Although these theories are not directly extensible to our recovery problem, these theories reassure that extensions in Fourier space are possible, and hence the filled-in missing wedges may be trusted if the resultant structures in the real space appear plausible.

Another independent argument supporting why the missing wedges could correctly be filled can be given from a statistical viewpoint. Recall that the regularization used in the ER-DC

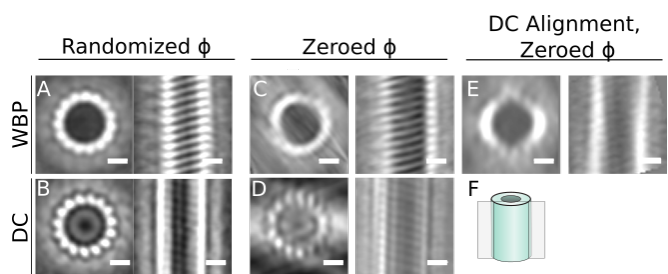


Fig. 7. Subtomogram analysis of WBP and DC-processed microtubule. In all panels, top and side views of the average are shown for the microtubule average obtained under the specified conditions (A) Average from the WBP tomogram, using a randomized azimuth-angle (ϕ) averaging approach to compensate for the missing wedge (35). (B) Average from the DC tomogram using the same randomized ϕ scheme. (C) Average from the WBP tomogram, with initial constant ϕ angles for all particles, allowing the missing wedge to affect the average. (D) Average from the DC tomogram using the same constant ϕ scheme. (E) Average generated by applying the alignment parameters from the DC uniform starting azimuth/restricted rotation alignment to the WBP particles. (F) Schematic showing the location of the slice on the right-hand side image in each panel. Scale bars: 10 nm.

324 from a close smoothness parameter. These different DC images
325 are studied side-by-side comparing 3-dimensional volumes for
326 details. The side-by-side images are very similar to one another,
327 but subtle features between them exist. Crucial are the
328 orthogonal Z image planes for judging smoothness parameters
329 and structure. There are a number of considerations for the
330 DC process, discussed in the supporting information.

331 How does one know if the DC structure is credible? In
332 addition to the side-by-side study of several smoothness DC
333 images, a control raw WBP image must be studied alongside
334 the DC images, at several intensity scalings of the WBP data.
335 Any feature uncovered in the DC data would be searched for
336 in the raw WBP data control, and would have to be present
337 in the WBP control. However, in our experience, the DC
338 process has never been observed to invent a structure that is
339 not present in the WBP raw data control. (26).

340 This study makes the statement that the missing wedge
341 of information is substantially filled by DC. Visually and in
342 Fourier space representation this is the case; however, this
343 statement needs caution. We do not know if DC will improve
344 Z resolution for certain kinds of data, intensities, or different
345 structures *e.g.*, of various sizes. It is possible that spaced
346 periodic structures position on top of one another along Z in
347 a tomogram are not resolved correctly in the DC data.

348 A second point in the DC discussion centers on what math-
349 ematics allows unobserved data to propagate from areas of

enforces certain hypothesized joint distribution of intensity and second-order derivative magnitude. It turns out that the back projected images deviate significantly from this joint distribution. Hence, the minimization involved in ER-DC brings in a proper filling on the wedges such that: 1) the resulting real space image is consistent with the measured projections, and 2) the resulting real space image better matches with hypothesized distribution.

Thirdly, DC could have an impact on the electron dose required to obtain a suitable tomogram. Because only one tilt axis for the tomogram is necessary to largely fill in the missing wedges, multi-axis tilt schemes meant to minimize the missing wedge become unnecessary. The DC process might allow other dose reduction steps, such as fewer tilts and lower beam intensity. In addition, there are several aspects of the DC process that can be improved, and are described in the supporting information.

The DC process filling in the missing wedges in Fourier space allows biological structures to be followed in 3-dimensions. This resolution is adequate to see, for example, gaps between the 10 nm nucleosomes allowing a chromosome path to be followed. One imagines a two step process for cellular tomography: first, the path of a structure is followed with the architecture discerned, a process greatly improved by DC. Subsequently, once an architecture is determined, molecular features can be superimposed using averaging methods and molecular modelling (35).

Materials and Methods

Sample Preparation. Yeast *S. cerevisiae* W303a cells were grown at 30°C in YPD media (1% yeast extract, 2% bacto-peptone, and 2% glucose) to mid-log phase, after which 5- μ L were deposited in a glow-discharged Quantifoil grid (200-mesh copper R2/1, Electron Microscopy Sciences), followed by manual blotting and plunge freezing in a 50/50 ethane propane mix (Airgas) using a custom-built manual plunger (Max Planck Institute of Biochemistry). Human Embryonic (HEK-293T) cells transfected with LRRK2-I2020T cells were prepared as described in (35). *In vitro* reconstituted LRRK2-I2020T was prepared as described in (53). For both yeast and HEK cells, frozen cells were micromachined on a Scios or an Aquilos 2 DualBeam FIB/SEM microscope (TFS). FIB milling was done as described in (6).

Cryo-electron tomography. Tilt series were obtained on a 300 kV Tecnai G2 Polara (TFS) or Titan Krios with a field emission gun, a GIF Quantum LS energy filter (Gatan) and a K2 Summit 4k \times 4k pixel direct electron detector (Gatan). Tilt series were acquired between $\pm 50^\circ$ and $\pm 70^\circ$ with increments of 2° and 3° , total electron doses between 70 and 100 $e^-/\text{\AA}^2$ at a target defocus of 5 μ m, and a pixel size of 2.2 or 3.5 \AA using the SerialEM software (60) in low-dose mode. Bidirectional or dose-symmetric tomography acquisition schemes were used (61), corrected for the pretilt of the lamella where appropriate. Images acquired on the K2 detector were taken in counting mode, divided into frames of 0.075 to 0.1 s.

Tomogram Reconstruction. Tilt series were aligned and dose-weighted by cumulative dose with MotionCorr2 (62). Dose-weighted tilt series were aligned and reconstructed using Etomo, part of the IMOD package (63). Patch tracking was

used to define the model for fine alignment. The aligned tilt series were reconstructed using weighted back projection to generate the 3D tomograms.

Deconvolution. A set of synthetic projections was generated with x and y dimensions and pixel spacing matching the reconstructed volume that will be deconvolved. Each projection has a centered point source that is then convolved with the inverse Fourier transform of the CTF, generated using the defocus and astigmatism parameters estimated by CTFFIND4 (17). The convolved point source/CTF is then reconstructed using the same elliptically weighted back projection used to generate the target reconstructed volume. Finally, the reconstruction is cropped to the same dimensions as the volume to be deconvolved, the 3D FFT of which will be used as the final PSF. Deconvolution is then run for 100 cycles using the PSF generated. A detailed description of the deconvolution procedure can be found in the supporting information.

Subtomogram Analysis. Microtubules filaments were traced in Dynamo to define coordinates and orientation. Single particles were defined every 4 nm along the filament, and subtomograms with a side length of 66 nm were then extracted from both the back projected and the deconvolved tomograms using these coordinates. For both sets of particles, subtomograms were iteratively aligned over three rounds of two iterations each. The particles were aligned using a spherical alignment mask to minimize bias. For the first round, the alignment was constrained to a 180 degree cone aperture, with no flip allowed and 20 degrees of azimuthal rotation, corresponding to the third Euler angle. Rounds two and three used a 30 and 10 degree cone aperture, respectively, and an azimuthal search range of 10 and 2 degrees respectively. No symmetry was assumed in the alignment. For further details, see (35). To assess any compensation for the missing wedge, alignment was performed on particles with initial tables describing the particles orientation from 1) a blank table to set all particle orientations to zero, and 2) a random table assigning each particle a random orientation.

To calculate averages for the autophagosome crystal subunit in the WBP and DC tomograms, first 50 particles were identified manually in the deconvolved volume to generate an initial average. This initial average was used as a template for Dynamo's template matching functionality and used to search for similar particles. A cross correlation threshold of 0.38 was selected, below which many particles appeared as false positives by visual inspection. Using the coordinates and putative orientations from template matching, 82 particles were cropped from both the back projected and deconvolved volumes. A global alignment was used on each dataset in two (even and odd sets) using the Dynamo subtomogram alignment function. Each half dataset was averaged and the directional Fourier shell correlation (dFSC) between the resulting half-averages. The alignment angles from the deconvolved particles were then applied to the back projection particles to create the average shown in Fig. 5A and to the relative resolution by dFSC.

Acknowledgements

We are most indebted to Eric Branlund whose computational efforts made this work possible. We used samples and tomograms provided by Robert Buschauer, Reika Watanabe,

508 Colin Deniston and Andres Leschziner. We thank Drs. Yifan
509 Cheng (UCSF), David DeRosier (Brandeis & La Jolla), Robert
510 Stroud (UCSF), Susan Taylor (UC San Diego), and members
511 of the Villa lab for discussions and support. We thank the
512 Henriques Lab for the bioRxiv L^AT_EX template. ER Decon DC
513 software and extensive help documentation can be obtained
514 from Agard/Sedat at UCSF. This work was supported by an
515 NIH New Innovator Award (DP2 GM123494) and an NSF MRI
516 grant (DBI 1920374) to E.V., an NIH R35 grant to D.A.A.
517 (NIH R35GM118099) and private funds from J.S. ME is the
518 Sam and Ayala Zacks Professorial Chair and head of the Irving
519 and Cherna Moskowitz Center for Nano and Bio-Nano Imag-
520 ing. We acknowledge the use of the UC San Diego cryo-EM
521 facility, which was built and equipped with funds from UC San
522 Diego and an initial gift from Agouron Institute, and of the
523 San Diego Nanotechnology Infrastructure (SDNI) of UC San
524 Diego, a member of the National Nanotechnology Coordinated
525 Infrastructure, supported by the NSF grant ECCS-1542148.

- 526 1. Villa E, Schaffer M, Plitzko JM, Baumeister W (2013) Opening windows into the cell:
527 focused-ion-beam milling for cryo-electron tomography. *Current Opinion in Structural Biol-*
528 *ogy* 23(5):771–777.
- 529 2. Marko M, Hsieh C, Schalek R, Frank J, Mannella C (2007) Focused-ion-beam thinning
530 of frozen-hydrated biological specimens for cryo-electron microscopy. *Nature Methods*
531 4(3):215–217.
- 532 3. Rigort A, et al. (2012) Focused ion beam micromachining of eukaryotic cells for cryoelec-
533 tron tomography. *Proceedings of the National Academy of Sciences of the United States of*
534 *America* 109(12):4449–4454.
- 535 4. Harapin J, et al. (2015) Structural analysis of multicellular organisms with cryo-electron to-
536 mography. *Nature Methods* 12(7):634–636.
- 537 5. Schaffer M, et al. (2019) A cryo-fli-
538 out technique enables molecular-resolution cryo-
539 et within native caenorhabditis elegans tissue. *Nature Methods* 16(8):757–762.
- 540 6. Wagner FR, et al. (2020) Preparing samples from whole cells using focused-ion-beam milling
541 for cryo-electron tomography. *Nature Protocols* 15(6):2041–2070.
- 542 7. Chang YW, Shaffer CL, Rettberg LA, Ghosal D, Jensen GJ (2018) In vivo structures of the
543 helicobacter pylori cag type iv secretion system. *Cell Reports* 23(3):673–681.
- 544 8. Lubit V, Leis A, Baumeister W (2008) Cryo-electron tomography of cells: connecting structure
545 and function. *Histochem Cell Biol* 130:185–196.
- 546 9. Ke Z, et al. (2018) Promotion of virus assembly and organization by the measles virus matrix
547 protein. *Nature Communications* 9(1):1–10.
- 548 10. Frank J (2006) *Introduction: Principles of electron tomography*. (Springer New York) Vol.
549 9780387690087, pp. 1–15.
- 550 11. Briggs JA (2013) Structural biology in situ—the potential of subtomogram averaging. *Current*
551 *Opinion in Structural Biology* 23(2):261–267.
- 552 12. Zhang P (2019) Advances in cryo-electron tomography and subtomogram averaging and
553 classification. *Current Opinion in Structural Biology* 58:249–258.
- 554 13. Baker LA, Rubinstein JL (2010) Radiation damage in electron cryomicroscopy. *Methods in*
555 *Enzymology* 481(C):371–388.
- 556 14. Erickson HP, Klug A (1970) The fourier transform of an electron micrograph: Effects of defo-
557 cussing and aberrations, and implications for the use of underfocus contrast enhancement.
558 *Berichte der Bunsengesellschaft für physikalische Chemie* 74(11):1129–1137.
- 559 15. Erickson HP, Klug A (1971) Measurement and compensation of defocusing and aberrations
560 by fourier processing of electron micrographs. *Philosophical Transactions of the Royal Society*
561 *of London. B, Biological Sciences* 261(837):105–118.
- 562 16. Wade RH (1992) A brief look at imaging and contrast transfer. *Ultramicroscopy* 46(1–4):145–
563 156.
- 564 17. Rohou A, Grigorieff N (2015) Ctfind4: Fast and accurate defocus estimation from electron
565 micrographs. *Journal of Structural Biology* 192(2):216–221.
- 566 18. Turk M, Baumeister W (2020) The promise and the challenges of cryo-electron tomography.
567 *FEBS Letters* 594(20):3243–3261.
- 568 19. Frangakis AS, Hegerl R (2001) Noise reduction in electron tomographic reconstructions using
569 nonlinear anisotropic diffusion. *Journal of Structural Biology* 135(3):239–250.
- 570 20. Fernández JJ, Li S (2003) An improved algorithm for anisotropic nonlinear diffusion for de-
571 noising cryo-tomograms. *Journal of Structural Biology* 144(1–2):152–161.
- 572 21. Buchholz TO, Jordan M, Pignio G, Jug F (2019) Cryo-care: Content-aware image restoration
573 for cryo-transmission electron microscopy data. (IEEE Computer Society), Vol. 2019–April,
574 pp. 502–506.
- 575 22. Huang X, Li S, Gao S (2018) Exploring an optimal wavelet-based filter for cryo-et imaging.
576 *Scientific Reports* 8(1):2582.
- 577 23. Tegunov D, Cramer P (2019) Real-time cryo-electron microscopy data preprocessing with
578 warp. *Nature Methods* 16(11):1146–1152.
- 579 24. Dougherty RP (2005) Extensions of damas and benefits and limitations of deconvolution in
580 beamforming. (AIAA International), Vol. 3, pp. 2036–2048.
- 581 25. Sage D, et al. (2017) Deconvolutionlab2: An open-source software for deconvolution mi-
582 croscopy. *Methods* 115:28–41.
- 583 26. Waugh B, et al. (2020) Three-dimensional deconvolution processing for stem cryotomography.
584 *Proceedings of the National Academy of Sciences* 117(44):27374–27380.
- 585 27. Bepler T, Kelley K, Noble AJ, Berger B (2020) Topaz-denoise: general deep denoising models
586 for cryoem and cryoet. *Nature Communications* 11(1):1–12.
- 587 28. Yan R, Venkatakrisnan SV, Liu J, Bouman CA, Jiang W (2019) Mbir: A cryo-et 3d recon-
588 struction method that effectively minimizes missing wedge artifacts and restores missing in-
589 formation. *Journal of Structural Biology* 206(2):183–192.
- 590 29. Gibson SF, Lanni F (1992) Experimental test of an analytical model of aberration in an oil-
591 immersion objective lens used in three-dimensional light microscopy. *Journal of the Optical*
592 *Society of America A* 9(1):154.
- 593 30. Swedlow J, Sedat J, Agard D (1997) Deconvolution in optical microscopy in *Deconvolution of*
594 *Images and Spectra, 2nd edition*, ed. Jansson P. (Academic Press, San Diego), 2nd edition,
595 pp. 284–309.
- 596 31. Kam Z, Hanser B, Gustafsson MG, Agard DA, Sedat JW (2001) Computational adaptive
597 optics for live three-dimensional biological imaging. *Proceedings of the National Academy of*
598 *Sciences of the United States of America* 98(7):3790–3795.
- 599 32. Jansson P (1997) *Deconvolution of images and spectra*. (Academic Press, New York), 2nd
600 edition.
- 601 33. Arigovindan M, et al. (2013) High-resolution restoration of 3D structures from widefield im-
602 ages with extreme low signal-to-noise-ratio. *Proceedings of the National Academy of Sci-*
603 *ences of the United States of America* 110(43):17344–17349.
- 604 34. Ercius P, Alaidi O, Rames MJ, Ren G (2015) Electron Tomography: A Three-Dimensional
605 Analytic Tool for Hard and Soft Materials Research. *Adv Mater* 27(38):5638–5663.
- 606 35. Watanabe R, et al. (2020) The In Situ Structure of Parkinson’s Disease-Linked LRRK2. *Cell*
607 182(6):1508–1518.
- 608 36. Carlsson SR, Simonsen A (2015) Membrane dynamics in autophagosome biogenesis. *Journal*
609 *of Cell Science* 128(2):193–205.
- 610 37. Chen H, Clyborne WK, Sedat JW, Agard DA (1992) Prism: an integrated system for display
611 and analysis of 3-d microscope images, eds. Acharya RS, Cogswell CJ, Goldgot DB. (SPIE),
612 Vol. 1660, pp. 784–790.
- 613 38. Castaño-Díez D, Zanetti G (2019) In situ structure determination by subtomogram averaging.
614 *Science* 351(6276):969–972.
- 615 39. Mahamid J, et al. (2016) Visualizing the molecular sociology at the hela cell nuclear periphery.
616 *Science* 351(6276):969–972.
- 617 40. Hutchings J, Stancheva V, Miller EA, Zanetti G (2018) Subtomogram averaging of copii as-
618 semblies reveals how coat organization dictates membrane shape. *Nature Communications*
619 9(1):1–8.
- 620 41. Khoshouei M, Pfeffer S, Baumeister W, Förster F, Danev R (2017) Subtomogram analysis
621 using the volta phase plate. *Journal of Structural Biology* 197(2):94–101.
- 622 42. Grojahn DA, et al. (2018) Cryo-electron tomography reveals that dynactin recruits a team of
623 dyneins for processive motility. *Nature Structural and Molecular Biology* 25(3):203–207.
- 624 43. Ke Z, et al. (2020) Structures and distributions of sars-cov-2 spike proteins on intact virions.
625 *Nature* 588(7838):498–502.
- 626 44. Obr M, Schur FK (2019) Structural analysis of pleomorphic and asymmetric viruses using
627 cryo-electron tomography and subtomogram averaging. *Advances in Virus Research*
628 105:117–159.
- 629 45. Jiménez-Ortigoza C, et al. (2021) Preliminary structural elucidation of β -(1,3)-glucan syn-
630 thase from candida glabrata using cryo-electron tomography. *Journal of Fungi* 7(2):1–13.
- 631 46. Ferreira JL, et al. (2019) Gamma-proteobacteria eject their polar flagella under nutrient de-
632 pletion, retaining flagellar motor relic structures. *PLoS Biology* 17(3).
- 633 47. Turoňová B, et al. (2020) In situ structural analysis of sars-cov-2 spike reveals flexibility me-
634 diated by three hinges. *Science* 370(6513):203–208.
- 635 48. Lin J, Heuser Z, Carbajal-González BI, Song K, Nicastro D (2012) The structural heterogene-
636 ity of radial spokes in cilia and flagella is conserved. *Cytoskeleton* 69(2):88–100.
- 637 49. Fukuda Y, Beck F, Plitzko JM, Baumeister W (2017) In situ structural studies of tripeptidyl
638 peptidase ii (tppeii) reveal spatial association with proteasomes. *Proceedings of the National*
639 *Academy of Sciences of the United States of America* 114(17):4412–4417.
- 640 50. Asano S, et al. (2015) A molecular census of 26s proteasomes in intact neurons. *Chromosome*
641 *Research* 23(2):439–442.
- 642 51. Weiss GL, Kieninger AK, Maldener I, Forchhammer K, Pilhofer M (2019) Structure and func-
643 tion of a bacterial gap junction analog. *Cell* 178(2):374–384.e15.
- 644 52. Himes BA, Zhang P (2018) emclarity: software for high-resolution cryo-electron tomography
645 and subtomogram averaging. *Nature Methods* 15(11):955–961.
- 646 53. Deniston CK, et al. (2020) Structure of LRRK2 in Parkinson’s disease and model for micro-
647 tubule interaction. *Nature*.
- 648 54. Liao HY, Frank J (2010) Definition and Estimation of Resolution in Single-Particle Reconstruc-
649 tions.
- 650 55. Dang S, et al. (2017) Cryo-EM structures of the TMEM16A calcium-activated chloride channel.
651 *Nature* 552(7685):426–429.
- 652 56. Castaño-Díez D, Kudryashev M, Arheit M, Stahlberg H (2012) Dynamo: A flexible, user-
653 friendly development tool for subtomogram averaging of cryo-EM data in high-performance
654 computing environments. *Journal of Structural Biology*.
- 655 57. Goodman JW (1968) *Introduction to Fourier Optics*. (McGraw-Hill Companies, New York),
656 2nd edition, pp. 161–165.
- 657 58. Ye JC (2019) Compressed sensing MRI: a review from signal processing perspective. *BMC*
658 *Biomedical Engineering* 1(1):1–17.
- 659 59. Leary R, Saghi Z, Midgley PA, Holland DJ (2013) Compressed sensing electron tomography.
660 *Ultramicroscopy* 131:70–91.
- 661 60. Schorb M, Haberbosch I, Hagen WJ, Schwab Y, Mastrorade DN (2019) Software tools for
662 automated transmission electron microscopy. *Nature Methods* 16(6):471–477.
- 663 61. Hagen WJH, Wan W, Briggs JAG (2017) Implementation of a cryo-electron tomography tilt-
664 scheme optimized for high resolution subtomogram averaging. *J Struct Biol* 197(2):191–198.
- 665 62. Zheng SQ, et al. (2017) MotionCor2: anisotropic correction of beam-induced motion for im-
666 proved cryo-electron microscopy. *Nat Methods* 14(4):331–332.
- 667 63. Kremer JR, Mastrorade DN, McIntosh JR (1996) Computer visualization of three-
668 dimensional image data using IMOD. *J Struct Biol* 116(1):71–76.